GEOPHYSICAL EXPLORATION IN THE
XINGLIN BAY GEOTHERMAL FIELD, SE-CHINA

Xi Yufei

Institute of Hydrogeology and Environmental Geology
Chinese Academy of Geological Sciences
No.268, North Zhonghua Road, Shijiazhuang City
Hebei Province
CHINA
xiyufei2008@gmail.com

ABSTRACT

Xinglin Bay is a low-temperature geothermal field belonging to the Zhangzhou Basin geothermal area, one of the hottest geothermal areas in SE-China. In order to have a better understanding of the geothermal resource, MT and gravity data were processed and inverted and a joint interpretation with borehole data was carried out. Resistivity and density structures were studied and the surface heat flow was calculated. Geological structures were studied with geophysical work. Intrusive rocks show high resistivity and high density features. The borehole logs indicate that the regional temperature gradient is not as high as reported before. The occurrences of local natural springs are closely related to intrusions and faults. TEM work is recommended together with MT work to correct the static shift of MT data. Current geophysical work is not conclusive for geothermal exploration. Temperature gradient surveys are recommended before planning to drill deep boreholes.

1. INTRODUCTION

Xinglin Bay geothermal prospect belongs to the Zhangzhou Basin geothermal area, located on the coastline of SE-China. Zhangzhou Basin is one of the most important geothermal fields in China and it is endowed with numerous natural thermal springs. Zhangzhou, Xiamen and Quanzhou, called the Minnan Golden Triangle, is a highly industrialized region and the air quality is one of the best of all regions in China (AQICN, 2018). The highest temperature of the natural springs in Zhangzhou Basin is 106°C (Figure 1), and 121.5°C at the bottom of a 90 m deep borehole (Xiong et al., 1990a). It is also the hottest geothermal field in SE-China. The geothermal fields of this region are of medium- to low-temperature type, mainly distributed along faults. The Xinglin Bay geothermal field is located in the northeast part of Zhangzhou Basin geothermal field (Figure 1), between Xinglin town and Xiamen city. Three hot springs with temperatures of 66°C, 89°C, and 73°C are found in the study area, arranged in W-E direction. The spring water is clear but salty and smelly.

Previous studies indicate that the temperature gradient and heat flow in Zhangzhou Basin are 85-162°C/km. and about 120 mW/m^2, respectively (Wang and Huang, 1990; Yuan et al., 2006). Geophysical studies have been conducted in Zhangzhou Basin since the 1980s. Studies of receiver functions (techniques to study the velocity structure of Earth based on information from teleseismic
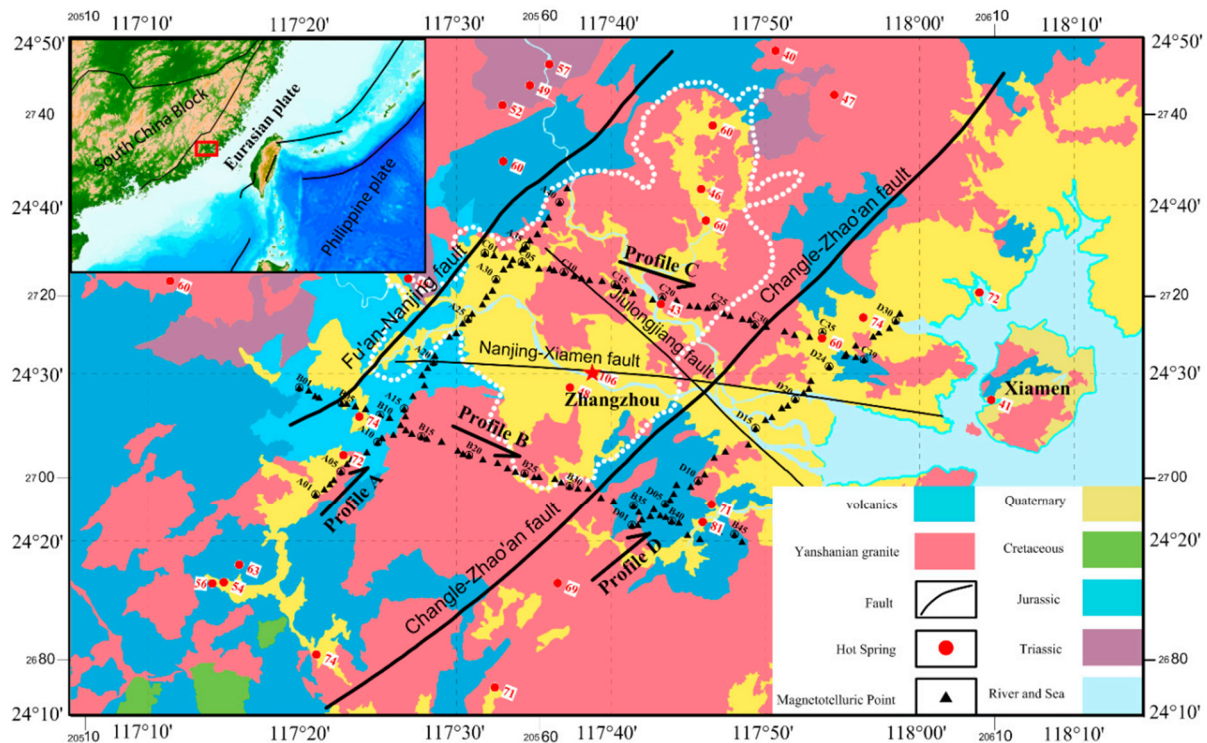
FIGURE 1: Geological map of the study area and surrounding region; the black square is the
study area. The location of MT sites, hot springs and their temperatures, geology and
tectonic settings are shown (revised from Wu et al., 2018)

earthquakes recorded at three-component seismic stations) show crustal thickness of about 30 km in the
study area and the crust becomes thinner going from the mainland to the sea (Ai et al., 2007). A low P-
wave velocity layer which is about 3.0-4.0 km thick and with a velocity of 5.5-5.9 km/s has been found
in the middle crust of this region by a wide-angle seismic study (Liao et al., 1988). This is interpreted
as a ductile shear zone or the presence of partially molten rock (Yuan et al., 1989; Zhang and Wang,
2007). Previous magnetotelluric (MT) work, mainly for regional research, suggests that the
asthenosphere is shallow under the Zhangzhou Basin (Liu et al., 2012).

In order to have a better understanding of the formation of Zhangzhou geothermal field, comprehensive
geological work was designed by the Institute of Hydrogeology and Environmental Geology, Chinese
Academy of Geological Sciences. MT and gravity work was carried out by China University of
Geosciences between September 2016 and January 2017. The MT result was published in Wu et al.
(2018), which shows a low-resistivity layer in the middle crust. The drilling of a borehole in the Xinling
Bay geothermal field was finished in June 2017. Temperature and resistivity logging was conducted
later. The MT and gravity data near the borehole are processed in this report and compared with the
logging results. The resistivity and density structures are studied and surface heat flow is calculated.
Resistivity structure is not very clear due to low quality data. The results show that the regional
geothermal heat flow is not as high as reported before and the existence of local natural springs are
closely related to intrusions and faults.

2. GEOLOGICAL BACKGROUND

Zhangzhou Basin geothermal area, belonging geologically to the South China Block, is located on the
continental margin of the western Pacific Plate (Figure 1). The present South China tectonic framework
is controlled by complex interactions between the Eurasian plate, paleo-Pacific Ocean plate, the

Philippine Sea plate and the Indian plate. This region has experienced multiple tectonic events since the Paleozoic, such as the Indosinian (late Permian-middle Triassic) orogeny and the Yanshanian (Jurassic-Cretaceous) tectono-magmatic events. The Yanshanian movement, a counter clockwise rotation of the Chinese continent with westwards subduction and compression of the Okhotsk and Izanagi plate, 205 - 135 Ma (Mesozoic time) (Wan, 2012), was the peak period of the tectonics and resulted in thinned lithosphere (Zhou et al., 2012) and extensive Mesozoic granite, widely distributed with Jurassic volcanic rock as a covering layer (Zhou et al., 2006).

Figure 2 shows a local geological map. The surface stratum consists of Jurassic and Quaternary formations:

1) The Jurassic Upper Tongnanyuan formation (J): It is mainly a sequence of strata originating from volcanic eruptions. The lithology is mainly rhyolite, tuff, lava, sandstone, mud stone, etc. These are often the surrounding rock of the early and late Yanshanian intrusive rocks.

2) Quaternary (Q): The Quaternary strata in the survey area are mainly distributed at the rivers on the banks of the central part and in the estuary, coastal plains, peninsula, piedmont and inter-mountain basins, forming the major topography below 50-60 m.

Intrusive rocks in the study area are widely distributed, including: the biotite granite intrusion in the early Yanshanian time (Jr) and the late Yanshanian (Kr) monzonitic granite. The intrusions form a hilly landform. In addition to the above-mentioned rock masses, there are different stages of rock veins exposed along both sides of fault zones. Faults are well developed with northeasterly and northwesterly major directions (Figure 2). The Pingtan-Dongshan fault (F1) and Shiweitou-Gaoqi fault (F3) intersect in the eastern part of the study area. The distribution of natural hot springs is dominated by the Yanshanian magmatic intrusions. These deep faults and intrusions play an important role in the geothermal activity.
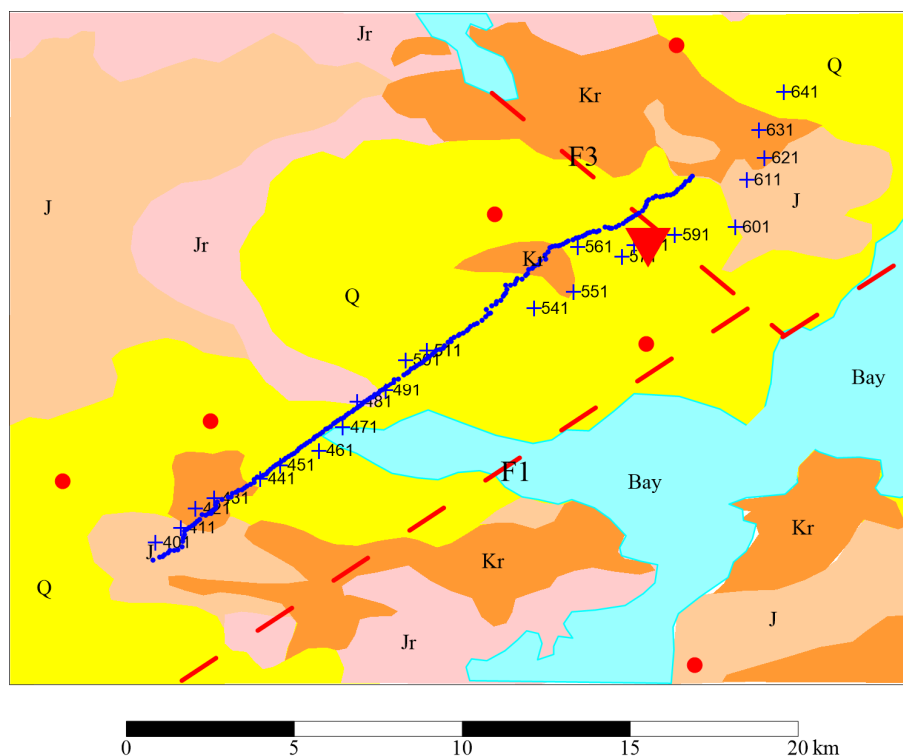

FIGURE 2: Geological map of the study area. J: Jurassic strata; Jr: Jurassic intrusion;
Q: Quaternary sediment; Kr: Cretaceous intrusion. Blue crosses are locations of MT stations,
blue dots are positions of gravity stations, red dots are natural springs, red inverse triangle
is the position of the borehole and red broken lines are faults

3. GEOPHYSICAL METHODS IN GEOTHERMAL EXPLORATION AND SCOPE OF WORK

The exploration of geothermal resources is the basis for their development. Surface geology and geochemistry are always limited to direct observation on surface, while geophysics can penetrate much deeper. Geophysical methods have been widely used in geothermal surveying and development. The task in geothermal exploration is the detection and delineation of geothermal resources and the understanding of their characteristics, the location of exploitable reservoirs and the siting of boreholes through which hot fluids at depth can be extracted (Hersir and Björnsson, 1991). The principle of geophysical methods in geothermal exploration is to detect the parameters related to high-temperature rocks and fluids, or other parameters that reveal geological structures controlling geothermal activity.

Based on different purposes, geophysical methods are sometimes classified into two categories: direct methods for temperature and fluid detection and indirect methods for the related geological structure detection. Direct methods include temperature logging, resistivity methods (magnetotelluric sounding (MT); Transient Electromagnetics (TEM); Direct Current (DC); Alternative Current (AC)), passive seismics and self-potential (SP), while the indirect methods include potential field methods (magnetics and gravity), active seismic method, etc. Resistivity methods are generally considered as the most powerful geophysical prospecting method in geothermal exploration. Resistivity is highly sensitive to temperature, porosity, salinity of water and geothermal alteration processes and directly related to parameters characterizing the geothermal reservoir. Seismic methods give important structural information that can be directly related to the flow of water within the geothermal reservoir. Micro-seismicity can delineate active faults and the ductile/brittle boundary.

Main geological parameters of the geothermal reservoir to be determined by indirect methods are: geological formation (lithology), tectonic structures (faults), intrusions and stress field etc. Gravity anomalies reflect lateral variations of density in the crust and are used to study geological features such as faults and dikes, basement depth variations, rims of calderas, intrusions, rock alteration and porosity variations. The magnetic method is used for locating intrusions, dykes, faults, buried lava and hydrothermally altered rocks. Seismic methods are used to study the elastic parameters at depth, and can image the basement, geological formations, the presence and geometry of faults, etc.

Gravity and MT work has been carried out on a profile in the study area (Figure 2). The direction of the profile is northeast, almost perpendicular to the F3 fault (Figure 2). Gravity and MT stations are not co-located, as MT stations extend further than the gravity stations. Both the gravity and MT data are projected to the same profile (Figure 2). Intrusions crop out on the profile at 2.5-4.5 km, 8-9 km and 15-16 km. Natural springs are located at 5 km and 16 km, along the profile.

Data from a total of 157 broadband (320-0.00055 Hz) MT sites were collected in the Xinglin Bay geothermal field using Phoenix MTU Instruments, 21 stations near the borehole are considered in this work. The horizontal electric (E_x, E_y) and magnetic (H_x, H_y) field components were measured in magnetic N-S and magnetic E-W with a site spacings of 1-2 km (Wu et al., 2018). The distance between gravity stations is about 100 m. A total of 204 stations were collected.

4. THE MT METHOD

4.1 Resistivity of rocks

Resistivity of a material is defined through electrical resistance by Ohms law. For a conducting cylinder, the resistivity is given by:

$$\rho = R \cdot S / L \qquad (1)$$

where ρ is the specific resistivity of the material (Ωm), R is resistance (Ω), L is length (m) and A is cross-sectional area (m^2).

The specific resistivity ρ relates current density and electric field by:

$$\rho \boldsymbol{j} = \boldsymbol{E} \tag{2}$$

where $\boldsymbol{E}$ is electric field (V/m), and $\boldsymbol{j}$ is current density (A/m^2).

The specific resistivity of rocks is affected by several parameters of the geothermal system like temperature, fluid type and salinity, porosity, composition of the rocks, and the presence of alteration minerals. For low-temperature geothermal fields, the major factors should be the presence of fluid (permeability), porosity, composition of rocks, salinity and temperature.

4.2 Basics of MT

Magnetotellurics (MT) is a passive (natural source) electromagnetic sounding method that uses natural electromagnetic fields to investigate the resistivity structure of the earth (Vozoff, 1991). The fluctuating natural magnetic field induces electrical currents in the conductive ground. By measuring the fluctuating magnetic field and the electrical currents (i.e. the electrical field) simultaneously in orthogonal directions on the surface of the earth, it is possible to infer the subsurface resistivity. The varying electric and magnetic fields are coupled through the Maxwell's equations:

$$\nabla \times \boldsymbol{E} = -\frac{\partial \boldsymbol{B}}{\partial t} \tag{3}$$

$$\nabla \times \boldsymbol{H} = \boldsymbol{j} + \frac{\partial \boldsymbol{D}}{\partial t} \tag{4}$$

$$\nabla \cdot \boldsymbol{B} = 0 \tag{5}$$

$$\nabla \cdot \boldsymbol{D} = \eta \tag{6}$$

where
$\boldsymbol{E}$ = Electrical field intensity (V/m);
$\boldsymbol{B}$ = Magnetic induction (T);
$\boldsymbol{H}$ = Magnetic field intensity (A/m);
$\boldsymbol{j}$ = Electrical current density (A/m^2);
$\boldsymbol{D}$ = Electric displacement (C/m^2);
η = Electric charge density owing to free charges (Cm^{-3}).

Constitutive relations are: $\boldsymbol{j} = \sigma \boldsymbol{E}$, $\boldsymbol{D} = \varepsilon \boldsymbol{E}$ and $\boldsymbol{B} = \mu \mathbf{H}$, where σ is electrical conductivity (S/m); $\rho = 1/\sigma$ or the electrical resistivity (Ωm),

In studying the main principles, we consider the case of an electromagnetic wave propagating through a homogeneous half-space of conductivity σ. The fields vary harmonically in time with angular frequency ω. In this case Equations 3-6 lead to:

$$\nabla^2 \boldsymbol{E} - k^2 \boldsymbol{E} = 0 \tag{7}$$

$$\nabla^2 \boldsymbol{H} - k^2 \boldsymbol{H} = 0 \tag{8}$$

where:

$$k^2 = \mu \varepsilon \omega^2 - i \mu \sigma \omega \tag{9}$$

and where μ is magnetic permeability, ε is the electric permittivity.

In the air we have σ = 0. But in the earth, because ε is negligible ($\sim 9\cdot10^{-12}$), the first term on the right side of Equation 9 can be omitted. We can calculate the velocity of the wave in the air, v_0, and in the half-space, v, getting:

$$v_0 = \frac{1}{\sqrt{\varepsilon_0\mu_0}} \ and \ v = \sqrt{\frac{2\omega}{\mu_0\sigma}} \tag{10}$$

If θ_i and θ_t are the incident and refraction angles, respectively, and v_0 and v are velocities in the air and the half-space, respectively, Snell's law gives:

$$\frac{1}{v_0}sin\theta_i = \frac{1}{v}sin\theta_t \tag{11}$$

By using Equation 10, we find that:

$$sin\theta_t = sin\theta_i\sqrt{\frac{2\varepsilon_0\omega}{\sigma}} \tag{12}$$

For $\rho < 10^4$ Ωm ($\sigma > 10^{-4}$ S/m) and $\omega < 10^3$ Hz:

$$\frac{2\varepsilon_0\omega}{\sigma} < 10^{-7} \tag{13}$$

Hence, θ_t is practically zero. The refracted waves will travel perpendicularly downwards into the half-space (the earth) for all incident angles and all derivatives with respect to horizontal coordinates vanish.

For a homogeneous earth, Equations 3 and 4 can be solved by using Equations 7-9 to find the impedance of an electromagnetic wave, which is the ratio of the orthogonal electric and magnetic fields

$$Z_{xy} = \frac{E_x}{H_y} = \frac{\omega\mu}{k} \tag{14}$$

$$Z_{yx} = \frac{E_y}{H_x} = -\frac{\omega\mu}{k} \tag{15}$$

This can be written as tensor equation:

$$\begin{bmatrix} E_x \\ E_y \end{bmatrix} = \begin{bmatrix} 0 & Z_{xy} \\ Z_{yx} & 0 \end{bmatrix}\begin{bmatrix} H_x \\ H_y \end{bmatrix} \tag{16}$$

where

$$Z_{xy} = -Z_{yx} \tag{17}$$

Equations 16 and 17 also hold for a layered (1D) earth where the conductivity changes only with depth but not in horizontal directions.

In the case of homogeneous earth, k in Equation 9 depends on the conductivity $\sigma=1/\rho$. Due to the smallness of ε, the first term on the right side of Equation 9 can be omitted and the Equations 14 and 15 can be solved for ρ and hence in terms of the off-diagonal tensor elements leading to:

$$\rho = \rho_{xy}(T) = 0.2T|Z_{xy}|^2 = 0.2T\left|\frac{E_x}{H_y}\right|^2 \tag{18}$$

where T is the period of the wave $T = 2\pi/\omega$.

Since k is a complex number the electric and magnetic fields in the earth are not in phase but with the phase difference:

$$\theta = \theta_{xy} = \arg(Z_{xy}) = \pi/4 \tag{19}$$

For a homogeneous earth, the resistivity and phase could also be calculated from the yx component of the tensor.

For a non-homogeneous earth, Equations 18 and 19 are used to calculate the apparent resistivity and phase as a function of T. For a homogeneous and 1D earth the apparent resistivity and phase are the same for the xy- and yx-polarisations, but for a more complicated resistivity structure, they will be different (Flóvenz et al., 2012). In the general case, the relations between the electric- and magnetic fields are given as:

$$\begin{bmatrix} E_x \\ E_y \end{bmatrix} = \begin{bmatrix} Z_{xx} & Z_{xy} \\ Z_{yx} & Z_{yy} \end{bmatrix} \begin{bmatrix} H_x \\ H_y \end{bmatrix} \tag{20}$$

Now there are several ways of defining the apparent resistivity and phases and they will depend on the orientation of the x- and y-axes.

For 1D inversion, as in this work, it is assumed that the earth is horizontally layered under each measuring site and that the apparent resistivity is independent of the orientation of the axes. In this case, it is customary to define the apparent resistivity and phase from a rotationally invariant combination of the tensor elements in Equation 20. One such is the determinant of the impedance tensor, leading to the following definition:

$$\rho_{det} = \frac{1}{\omega\mu_0}|Z_{det}|^2 = \frac{1}{\omega\mu_0}\left|\sqrt{Z_{xx}Z_{yy} - Z_{xy}Z_{yx}}\right|^2 \tag{21}$$
$$\theta_{det} = \arg(Z_{det})$$

The penetration depth of electromagnetic waves depends on two variables: the period of the wave and the resistivity where the wave is propagating. Long periods penetrate to greater depths than short periods. In a half-space of resistivity, ρ, the amplitude of a wave with period T will have decreased to 1/e of its original value on the surface at a depth (m) given by:

$$\delta = 503\sqrt{\rho T} \tag{22}$$

which is called the skin depth (Chave and Jones, 2012).

Consequently, short period (high frequency) waves contain near sub-surface information but are attenuated rapidly, while the long period (low frequency) waves can probe into deeper earth. Equation 22 can be used to estimate the depth of resolution of MT data.

The natural source signals used in MT surveys are generated in the atmosphere and magnetosphere. MT signals with frequency higher than 1 Hz are from thunderstorms near the equator. Signals less than 1 Hz are created through the interaction of solar wind interfering with earth's magnetic field. Dead band (low signal strength) for MT occurs in the frequency band ranging between 0.5 and 5 Hz (0.2 to 2 s) (Flóvenz et al., 2012).

In the MT method, two components of the electrical field (Ex, Ey) and three components of the magnetic field (Hx, Hy, Hz) are measured on the surface (Figure 3). The x-axis and the y-axis are normally taken to be magnetic N-S and magnetic E-W, respectively. Horizontal electric (**E**) and magnetic (**H**) fields are measured in the time domain and are transformed into the frequency domain using Fourier transformation in order to receive the MT response as a function frequency/period.
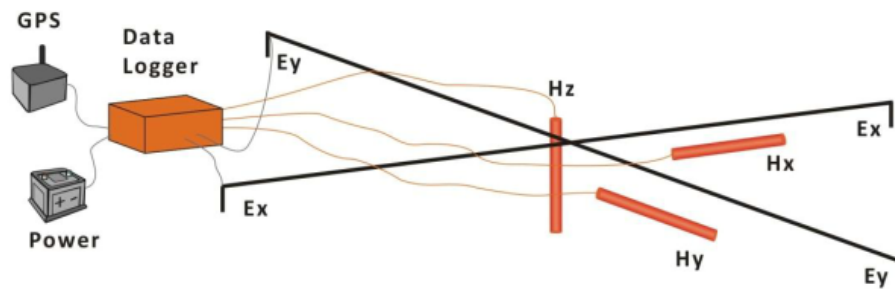
FIGURE 3: Layout of a magnetotelluric (MT) sounding (Flóvenz et al., 2012);
electrodes for measuring the electric field, coils for the magnetic field;
acquisition unit for digital recording and GPS clock for timing

4.3 Data acquisition

It is essential to acquire high quality data over a broad period range in MT data acquisition. The study area is located in a highly industrialized region, a lot of constructions and power lines are near the profile. Hence, noise from human activity in the MT data is inevitable (Figure 4). The easternmost sounding sites are only a few kilometres away from the southeast coastline of China. The large contrast in electrical conductivity between the seawater and land can distort the observed MT responses, especially when the separation distance from the coast is smaller than the skin depth of the frequency (Yang et al., 2010). This is generally known as sea effect. One possible approach to overcome this influence is to correct for the sea effect by an iterative method or to directly incorporate the sea into the models in the inversion (Lee et al., 2007; Unsworth et al., 2007). Average recording time for each station was over 20 hours.

FIGURE 4: MT working environment: a) Station 4491; b) Station 4541

4.4 Data processing

The main objective of MT data processing is to pick sets of smooth earth response functions from the time series signals.

4.4.1 Fourier transform

During the field work, MT data are recorded as a function of time (time series). The subsequent impedance and apparent resistivity calculations are performed in the frequency domain, so it is necessary to convert the electromagnetic field signal time series into a frequency domain signal. Fourier transformation is the basic method for obtaining spectral information. The Windows based Phoenix Geophysics software package SSMT2000 was used to do the Fourier transformation. Raw time series data, calibration data and site parameter files are the input data (Phoenix Geophysics, 2005)

4.4.2 Remote reference

The impedance tensor elements are calculated from auto- and cross-powers of the Fourier transforms of the electric and magnetic field components. Local correlated noise will contribute to the auto-powers and bias the tensor elements. Normally the basic magnetic field is similar over large distances but contaminated by local noise. To reduce the influence of the correlated noise in the auto-power spectrum, Gamble et al. (1979) proposed to correlate the Fourier spectra of the local MT site with the magnetic Fourier spectra from a simultaneously recording remote reference station with noise uncorrelated to the noise at the local station. This method was found to give much better results.

The remote sites must be chosen carefully in areas without noise. The method assumes that the earth's surface magnetic field is basically the same within appropriate distances (the range is related to the frequency of the magnetic field). The noise in the local and remote reference site is assumed to be uncorrelated and cancel out in the correlation. The remote reference calculations are conducted in the SSMT2000 Phoenix programme (Phoenix Geophysics, 2005). Figure 5 shows processed data from MT station 4451 with and without remote reference. Data quality is significantly improved with remote reference, especially in the intermediate frequency (dead band) 10-1 Hz, both the apparent resistivity and the phase are improved, and the curve shape is more realistic and smooth.

4.4.3 Data editing

Due to the local electromagnetic noises, it is inevitable to have certain errors in the measured data. In some of the cases presented here, the shape of the curve is changed, so noise must be removed before inversion. Generally, the curve smoothing process is adopted, mainly based on the following principles:

1) Smoothing should be done within the range of the error bar as much as possible;
2) The curve should be smoothed and outliers should be eliminated while maintaining the trend of the curve.
3) From the correspondence between the phase curve and the apparent resistivity curve, the abnormal points with no correspondence in phase are smoothed;
4) According to the smoothness of the measured curve and the principle of similarity of adjacent measuring points, the abnormal data points that are not similar to the adjacent measuring points are smoothed.

Figure 6 compares the apparent resistivity and phase before and after smoothing for station 4451. After the smoothing, the curve is more continuous, and especially the low-frequency data is improved. The smoothing process was conducted with the Phoenix program MTEditor (Phoenix Geophysics, 2005).
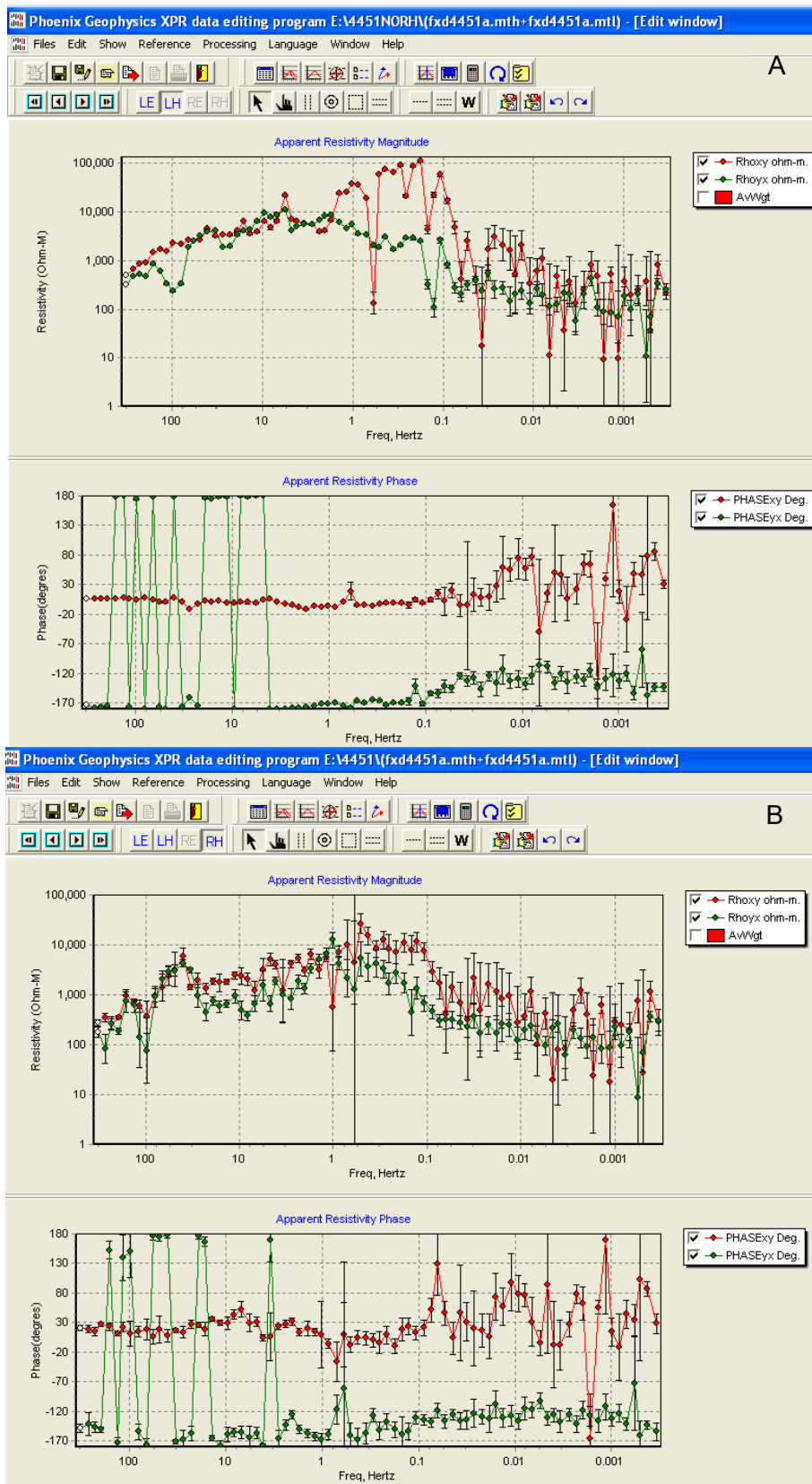
FIGURE 5: Comparison of remote reference method (before data editing):
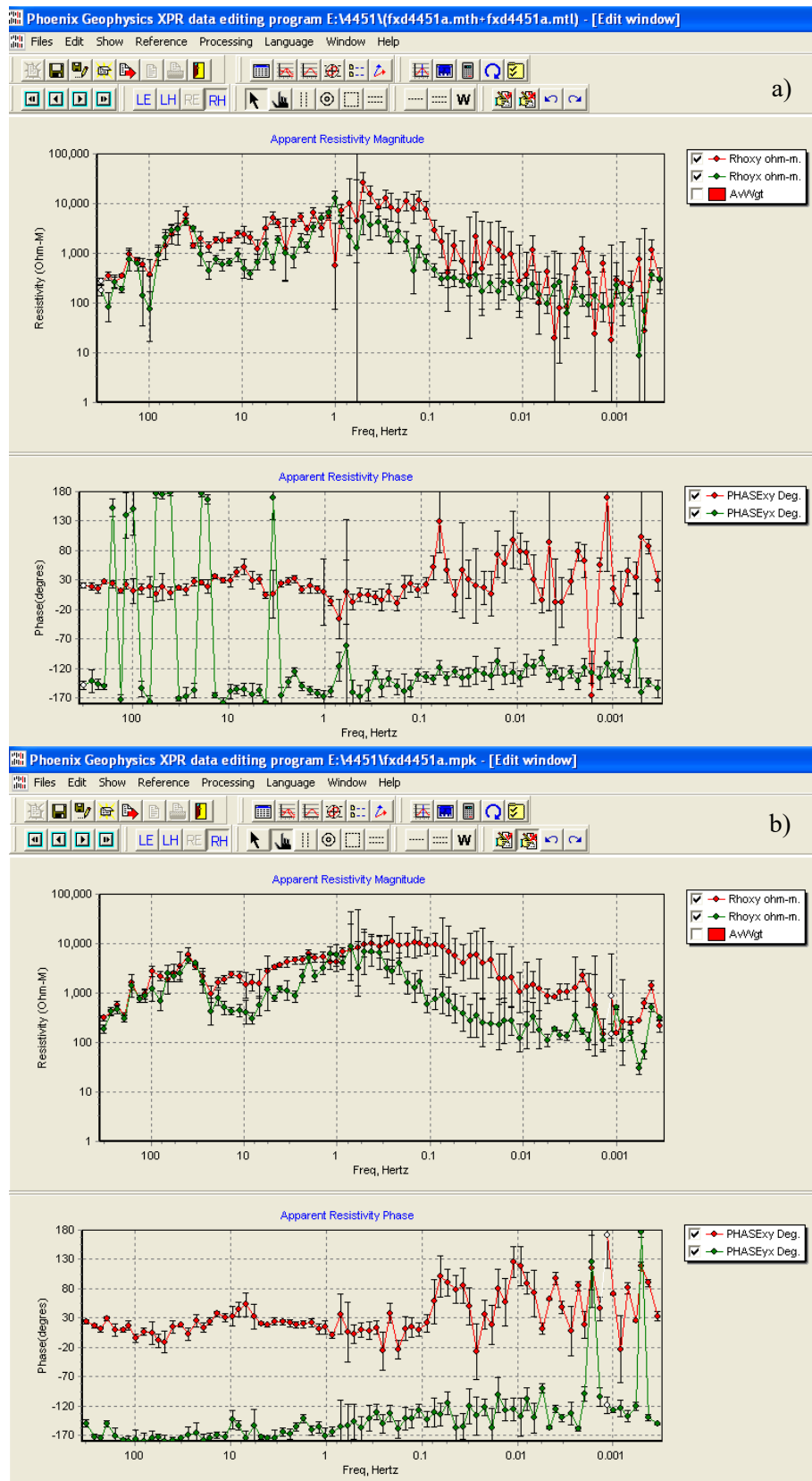a) Station 4451 without remote reference; b) Station 4451 with remote reference

FIGURE 6: Comparison of data editing: a) Station 4451 before data editing;
b) Station 4451 after data editing

4.5 Data inversion

4.5.1 1D OCCAM inversion with TEMTD

The 1D Occam inversion algorithm is a simple and effective inversion algorithm for obtaining smooth models (Constable et al., 1987). In 1D inversion it is assumed that the earth has horizontal layers with different resistivity, i.e. structure changes only with depth. In the 1D Occam inversion applied here, an initial model with many layers with fixed thickness, exponentially increasing with depth, is given and the inversion iteratively adjusts the resistivity of the layers to fit the measured data. Occam inversion means that the resistivity is constrained to vary smoothly with depth. The inversion was done using the TEMTD program, a 1D inversion code for TEM and MT data (Árnason, 2006). It can be used to invert TEM and MT data separately and also for joint inversion of TEM and MT data.

An initial thickness of the top layer, the number of layers and the basement depth of the model should be provided. Model parameters are the resistivity of the layers. Occam inversion is suitable for MT data as the skin depth increases with increasing period; high frequencies attenuate fast and sense small scale changes at the top of the model (thin layers at shallow depth) while long periods are sensitive to larger structures and reach deeper (thicker layers deeper down).

The inversion algorithm used in TEMTD is the Levenberg-Marquardt non-linear least-square inversion as described by Árnason (1989). The misfit function is the mean-square difference between measured and calculated values χ^2(*chi-squared*), weighted by the standard deviation of the measured values (Árnason, 2006). The best fit is obtained when the misfit function χ^2 (*chi-squared*) cannot be reduced further. The program offers the possibility to keep the models smooth, both with respect to resistivity variations between adjacent layers and layer thicknesses, if not fixed. The damping is achieved by utilizing both first order derivatives with respect to depth, which counteracts sharp steps in the model (on log scale) and second order derivatives, which counteract oscillations in the model values (on log scale), to obtain smooth models. The actual function that is minimized is not just χ^2, but the potential (P):

$$P = \chi^2 + \alpha D_{S1} + \beta D_{S2} + \gamma D_{D1} + \delta D_{D2} \tag{23}$$

where D_{S1} and D_{S2} are the first and second order derivatives of log-conductivities in the layered model and D_{D1} and D_{D2} are the first and second order derivatives of the logarithms of the ratios of layer depths. The coefficients, α, β, γ and δ are the relative contributions of the different damping terms and adjusted by the user.

Parameters used in the 1D inversion are: 40-50 layers, the depth to basement is about 100 km and top layer is 10 m thick. Resistivity value of the initial model is between 1 and 100 Ωm.

4.5.2 Static shift

The MT method suffers the static shift problem because the electric field is distorted by shallow resistivity anomalies close the electric dipoles. The term "static or telluric shift" is used because apparent resistivity is distorted by a multiplicative constant, *S*, and hence by a shift when presented on a log scale. The static shifts are mainly caused by electric field distortion due to dependency of electric field on resistivity and current distortion (current channelling /repelling). The apparent resistivity curve is shifted upwards above resistive bodies and downwards above conductive bodies.

Figure 7 illustrates the static shift effect due to a low resistive body (Árnason, 2015). When constant current density flows through 2D domains of different resistivity the electric field depends on the resistivity. In this example $\rho 2 < \rho 1$ and the electric field is smaller in the low resistivity domain. Unless at very high frequencies where eddy currents may be induced, this lowering of the electric field is independent of the frequency of the current. The apparent resistivity is given as:

$$\rho_{a1} = \frac{1}{\omega\mu}\left|\frac{E_1}{H}\right|^2 ; \quad \frac{1}{\omega\mu}\left|\frac{E_2}{H}\right|^2 = S \times \rho_{a1}; \quad S = \frac{\rho_2^2}{\rho_1^2} < 1 \qquad (24)$$

For the same magnetic field, the apparent resistivity will be lower in domain 2 than outside. If $\rho 1 > \rho 2$ the electric field and the apparent resistivity would be higher in the central domain than outside.
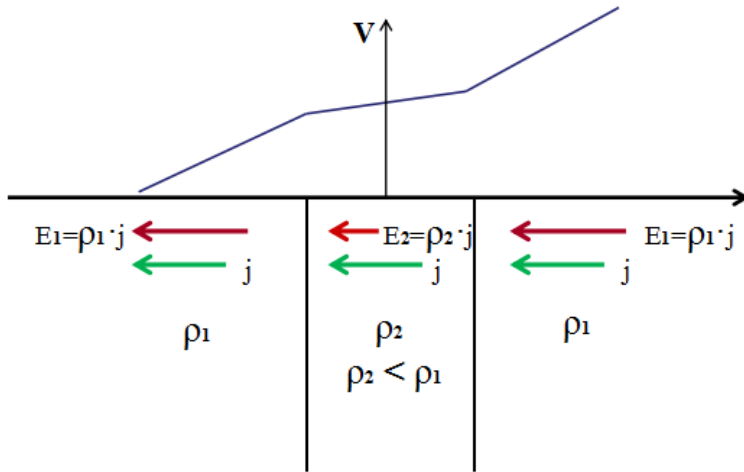

FIGURE 7: Electric field distortion causing static shift
(Árnason, 2015)

Static shift not only affects resistivity values, it also distorts the estimated depth to resistivity boundaries. A static shift multiplier (S) of less than 1 results in lower resistivity and decreased depth to boundaries and S higher than 1 results in higher resistivity and increased depth to boundaries.

Figure 8 shows the 1D inversion of the study profile with the static shift as 1 – no shift. It shows resistivity varying wildly along the profile. This is especially noticeable where a large body of low resistivity exists below 6 km depth under station 511, with an unlikely range between stations 561 and 591 because the MT soundings cannot resolve such local resistivity variations at this depth.
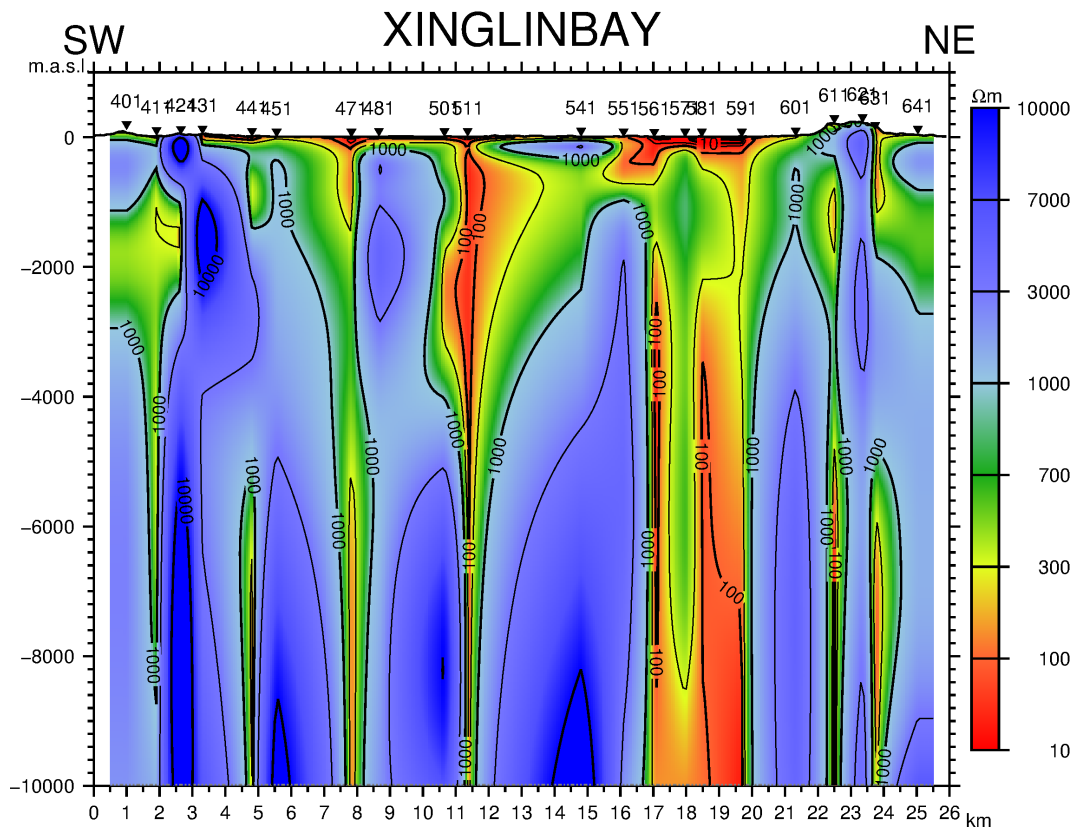

FIGURE 8: Resistivity cross-section using no static shift multiplier

Several ways of dealing with static shifts of MT data have been proposed. One solution is joint inversion of co-located TEM and MT data because TEM data is not affected by static shift (Árnason, 2015). Only MT work was carried out in this case, so TEM is not an option to improve the MT data quality. Therefore, manual adjustment was used. The basic principle for choosing the static shift multiplier is that the resistivity of horizontal layers near surface should be continuous. Vertical resistivity anomalies with small range at great depths are also very unlikely results, due to normal resolution of an MT survey, and should be eliminated. Different values of static shift were tested in our study, and values between 0.01 and 5 were used.

4.6 Results

Figure 9 shows an example of 1D Occam inversion of the MT data. A complete set of all the 1D inversion results is shown in the appendices to this report (Xi Yufei, 2018). On the right side is the resulting resistivity model with depth (green curve). Also shown are the values of chi and static shift. Only apparent resistivity data were used for inversion because the phase data were not of good quality.
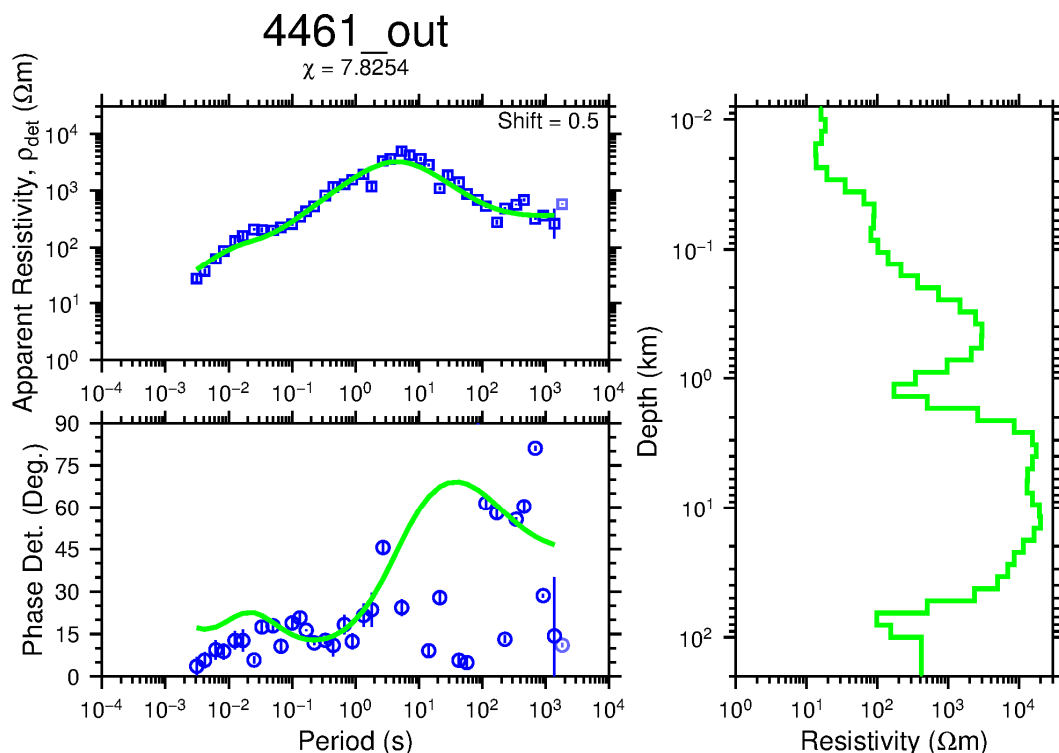

FIGURE 9: 1D inversion results of MT sounding 4461 using TEMTD. Blue symbols: apparent resistivity and phase derived from the determinant of the MT impedance tensor with vertical blue lines as error bars. Green lines in the panels to the left show the calculated response of the model to the right. Number on the top, 4461 is the name of the MT station; static shift multiplier is S=0.5 and the misfit (χ) is 7.8254

The MT results show the resistivity structure of Xinling Bay geothermal field (Figure 10). Electric resistivity ranges from 10 to 10,000 Ωm in the depth range down to 10 km. A low-resistivity layer (resistivity < 1000 Ωm and with a thickness of about 200 m) was inferred near the surface along the profile. Local geology suggests that the low-resistivity layer reflects Quaternary sediments and volcanic rocks of the late Jurassic. In general, resistivity increases from near surface to greater depths. A highly resistive region (> 10,000 Ωm) is found beneath the natural spring near station 541. There are three obvious high-resistivity regions below 5 km. One is found at 5-8.5 km along the profile. On the surface there are intrusive Cretaceous outcrops as shown by red crosses, with a natural thermal spring near the

intrusive rock close to station 431. Note that the positions of natural thermal springs are projected onto the profile. The real position is about 3 km to the northwest of the profile. The other two intrusions found between 14.7 and 22 km along the profile. Here, there is a Cretaceous intrusion outcrop on surface and a natural spring at 15.5-16 km. Finally, there are intrusive outcrops between 22 and 26 km, along the profile. This intrusion is associated with the high-resistivity body between 18.5 and 22 km.
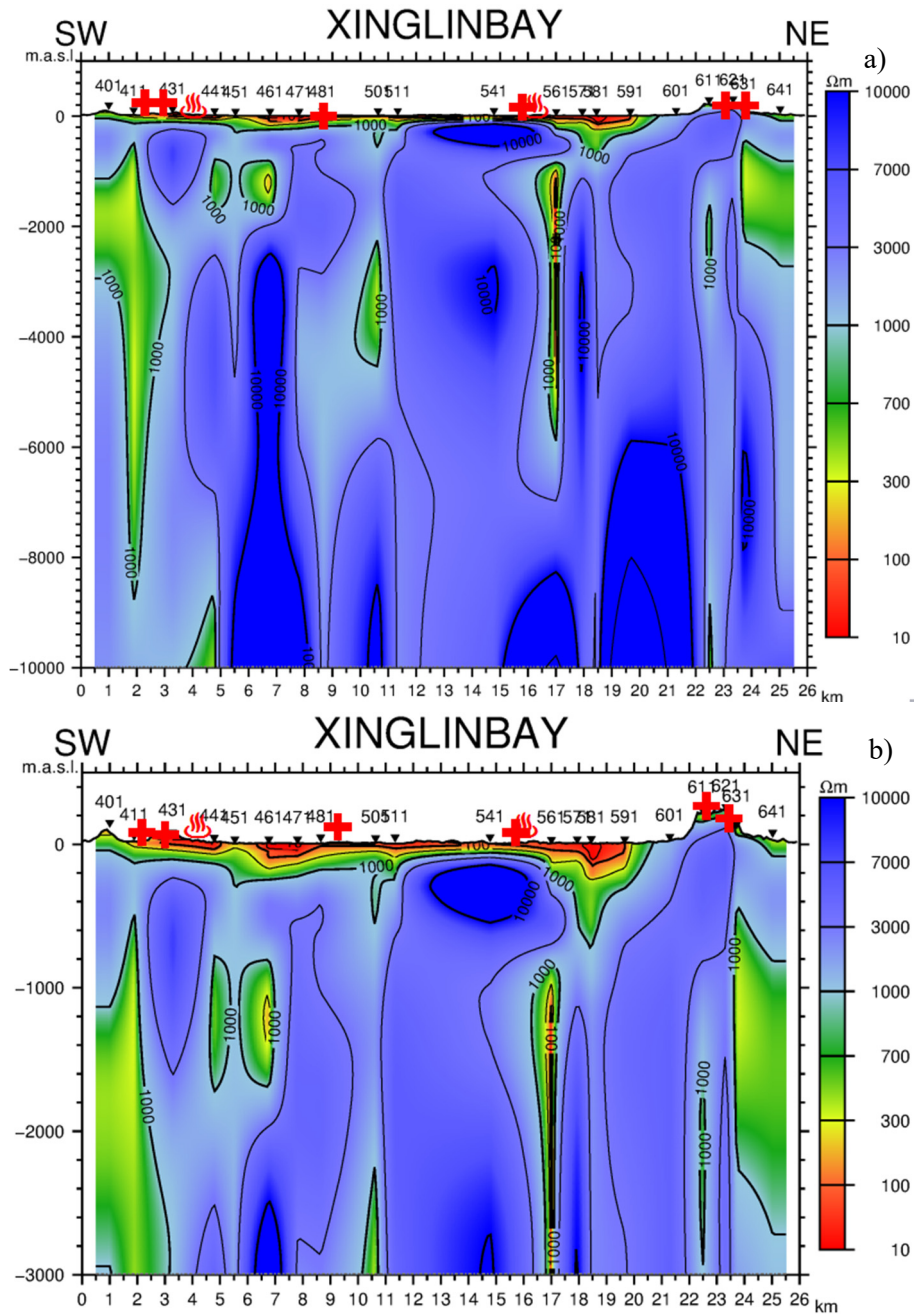
FIGURE 10: MT resistivity cross-section: a) Down to a depth of 10 km;
b) Down to a depth of 3 km;

♨ : Natural thermal spring   ✚ : Intrusive outcrops

5. GRAVITY WORK

5.1 Basic concepts

Surface gravity measurement is a passive method to investigate lateral subsurface density variations. It measures the gravitational acceleration on the surface with a gravimeter to investigate density variations in the earth, such as intrusions, buried faults, sedimentary basins, and undulation of crustal interfaces.

The principle of gravity methods is Newton's law of gravitational attraction: the force between two masses is proportional to each mass and inversely proportional to the square of their separation. Gravitational acceleration g of the earth is:

$$g = -\frac{GM}{R^2}$$ (24)

where G is the Newtonian constant of gravitation, approximately 6.674×10^{-11} N·kg^{-2}·m^2 in SI units; M is the mass of the earth; and R is the distance between the object and centre of earth.

Typical gravity value for gravitational acceleration is 9.8 m/s^2, between the extremes of 9.76 m/s^2 and 9.83 m/s^2 (Hirt et al., 2013). Earth's gravity is complex because:

1) The earth is not a sphere, but has an elliptical shape;
2) There is centrifugal force from the rotation of the earth; and
3) The earth has an irregular topography and density distribution.

Gravity anomalies result from the difference in density, or density contrast between a body and its surroundings strata. The density contrast and location determine the gravity anomaly. The density of rocks in the crust is between 1.5 and 3.3 g/cm^3, and depends on both their composition and porosity. Densities of rock samples in the study area are shown in Table 1. Sandstone from Jurassic time has a density of ~2.4 g/cm^3, while for quartz diorite from Cretaceous time it is 2.7 g/cm^3. Igneous rocks are denser than the strata in general.

TABLE 1: Density of samples in study area (Hu et al., 2017)

Rock type	Lithology	No. of samples	Density range (g/cm^3)	Average density (g/cm^3)
Late Jurassic strata	Dacite, volcanic tuff	30	~2.213-2.757	2.574
Early Jurassic strata	Sandstone	10	~2.370-2.462	2.418
Middle Jurassic strata	Quartz sandstone, siltstone	18	~2.371-2.559	2.430
Late Jurassic intrusive rock	Syenogranite	10	~2.530-2.598	2.565
Cretaceous intrusive rock	Quartz diorite	8	~2.702-2.764	2.740
Cretaceous intrusive rock	Alkali feldspar granite	7	~2.530-2.569	2.552
Cretaceous intrusive rock	Syenogranite	12	~2.584-2.673	2.626
Cretaceous intrusive rock	Granodiorite	6	~2.586-2.663	2.624

5.2 Data acquisition and reduction

Gravity data were collected on the surface with a CG-5 gravimeter from Scintrex Ltd., with a standard resolution of 1 mGal (1 mGal = 10^{-5} m/s^2). At an average interval of 100 m, 204 gravity stations were measured. Estimates of the elevation is often responsible for the greatest errors in the reduced gravity.

Recorded gravity data include the attraction of the reference ellipsoid, the effect of elevation above sea level, effect of "normal" mass above sea level, effect of tides, effect due to topography and effect of the

crust and mantle density variation (Blakely, 1995). The acceleration of gravity at the surface of the earth due to the whole mass of the earth is approximately 9.8 m/s^2 (980 Gal), whereas anomalies caused by crustal density variations are typically less than 10^{-3} m/s^2 (100 mGal), or less than 0.01% of observed gravity. Careful correction is necessary to remove various effects not related to the density of rock formations underlying the survey area. The Bouguer gravity anomaly is the most used presentation of gravity data, reduced from normal gravity, height where it is measured and the attraction of the terrain. It reflects "anomalous masses" of the crust.

The satellite Bouguer gravity anomaly in SE-China and the surrounding area is shown in Figure 11. This dataset is from the EGM 2008 model (Pavlis et al., 2012), based on the GRACE (Gravity Recovery and Climate Experiment) satellite mission. The gravity anomaly is negative on the mainland and positive on the sea, and about -10 - 0 mGal along the coastline in the southeast. The regional Bouguer anomaly reflects crustal thickness and density difference, negative Bouguer anomaly reflects a thick, low-density crust (Worzel and Shurbet, 1955). The minimum anomaly is -95 mGal in the northern mainland, maximum is about 50 mGal on the sea. The gravity anomaly increases gradually from northwest to southeast. An obvious gravity anomaly gradient exists on the coastline and crosses the study area. The gravity anomaly varies from -30 to 0 mGal along the gradient, and the horizontal gradient is about 0.8 mGal/km.
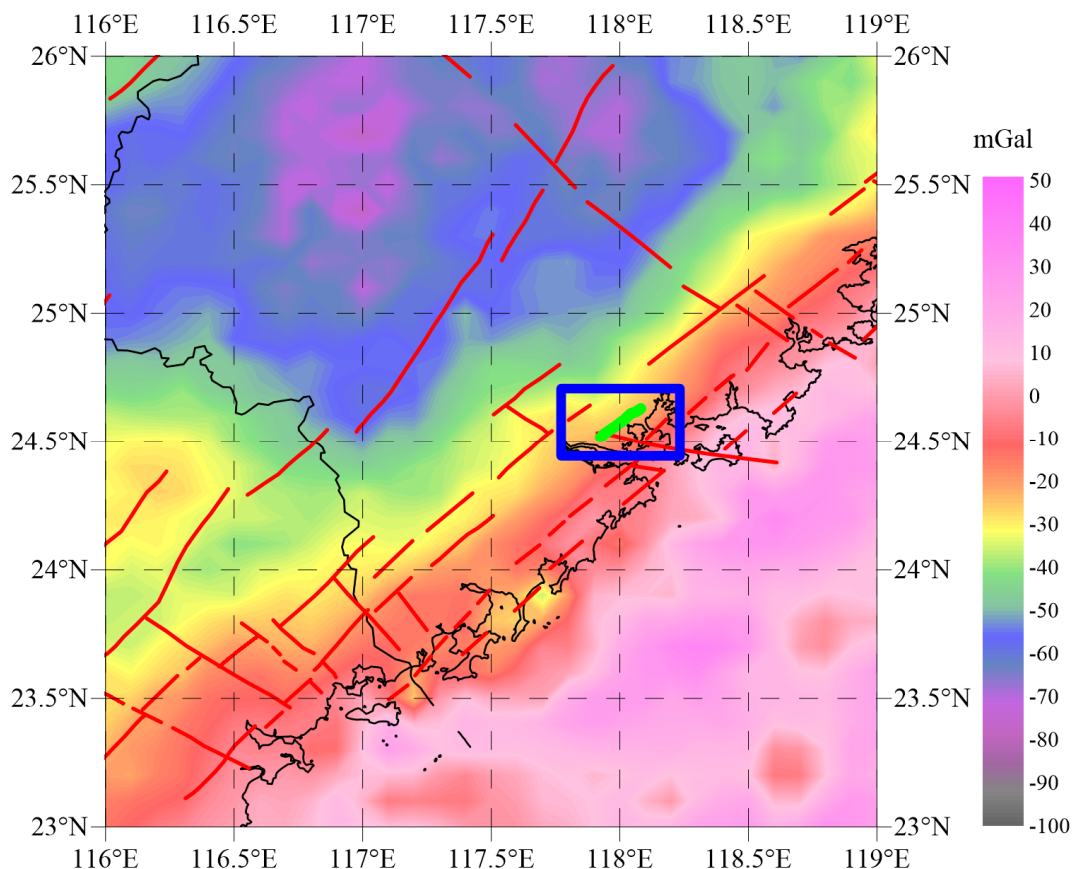

FIGURE 11: Satellite Bouguer gravity map showing the major faults in SE-China. The sea is in southeast part of the figure and the continent is in the northwest part. Black lines denote the coastline and provincial boundary. The blue square denotes the study area, the green line is the gravity profile and red lines are major faults

The gravity profile in this study (Figure 12) is perpendicular to the gravity gradient, and hence not affected by the crustal thickness variations. The Bouguer gravity anomaly along this profile mainly reflects local density anomalies and ranges from -32 mGal to -25.5 mGal. The highest value is about -25.5 mGal, at the southwest end of the profile, in Jurassic strata. The anomaly drops to about -28 mGal
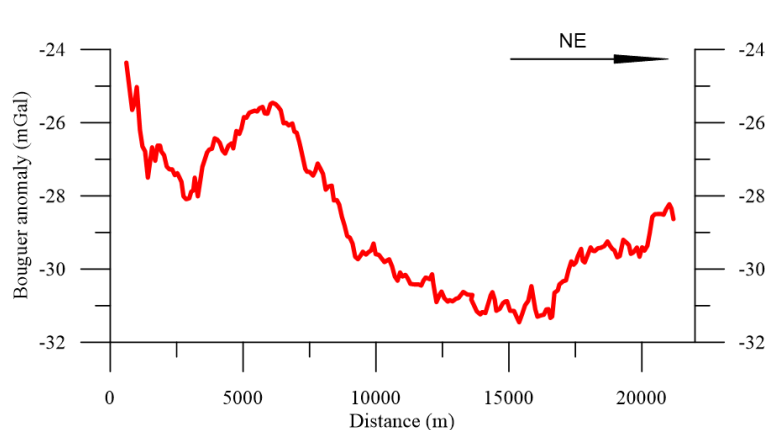
FIGURE 12: Bouguer gravity values along the
study profile shown in Figure 11

in the Cretaceous intrusion. The gravity values are fairly high between 3 and 10 km, where most of the outcropping strata is Quaternary sediments, except some small Jurassic intrusions located at around 7.5 km along the profile. The size of underground intrusions in the region is bigger than the surface exposure. Note that there is a surface geothermal manifestation located at 5 km along the profile, at a contact zone between the Cretaceous intrusion and Quaternary sediments, and the gravity values are anomalously high here. The values found between 10 and 16 km along the profile are relatively low, where most of the surface strata is Quaternary sediments. Then gravity values increase along the profile from 16 km to the northeast end, probably because of concealed intrusions.

5.3 Data processing

The Bouguer gravity anomaly reflects density anomalies from different depths. The regional anomaly is separated from the total anomaly with a moving average method and the depth to the source of the density anomaly is calculated with Euler deconvolution. Density tomography is obtained after the data have been inverted.

5.3.1 Moving average method

The moving average method is a common method for distinguishing local gravity field variations from the regional gravity field. The method averages the gravitational field over a moving window range, with the average as the regional value at the central point within the range. The difference between the observed value and the regional value is the local value. Local anomalies are caused by shallow subsurface structures and density variations. After the effects of the shallow subsurface material are averaged within a certain range, the local gravity anomalies are eliminated or attenuated. Obviously, the larger the window of average, the greater is the depth of bodies causing the surviving anomalies. Local anomaly reveals near-surface anomalies but the regional anomaly reveals deeper anomalies. In this study, the regional anomaly with 40 points window size contains information on intrusions (Figure 13). Regional anomaly with 10 points window size was used to estimate the depth to the source of the anomaly in Euler deconvolution.

5.3.2 Euler deconvolution

Euler deconvolution is a widely used method to estimate the position and depths of source in potential field data. The basic theory is given by (Reid et al., 1990; Thompson, 1982). This method relies on the fact that the gravitational field is represented by a homogeneous function. For such functions a certain relationship exists between the horizontal and vertical gradients of the field. By using horizontal gradients to estimate vertical gradients this relationship allows an estimate of the location of the field source. The method is independent of the size or density of the anomalous body, but it requires a parameter, the so-called "structural index", which depends on the assumed geometrical shape of the source. For a gravity field, it ranges from 0-2. The structural index is set as 1 for intrusions similar to a vertical cylinder (Geralda et al., 2004; Stavrev, 1997). In this study an x-gradient is run along the profile,

each giving an estimate of the source location. The results are shown as plusses in Figure 14. If the estimated source locations cluster in some regions, they are likely positions of sources of the field.

There are two major density sources in the Euler deconvolution results (Figure 14). One is at 7.5 km on the profile, with a depth down to its top about 3.8 km. The position coincides with the outcrop of the Jurassic intrusion in the sedimentary strata. The other is located between 15 and 18 km along the profile, at a depth of about 2 km. This coincides with the outcrop of the Cretaceous intrusion.
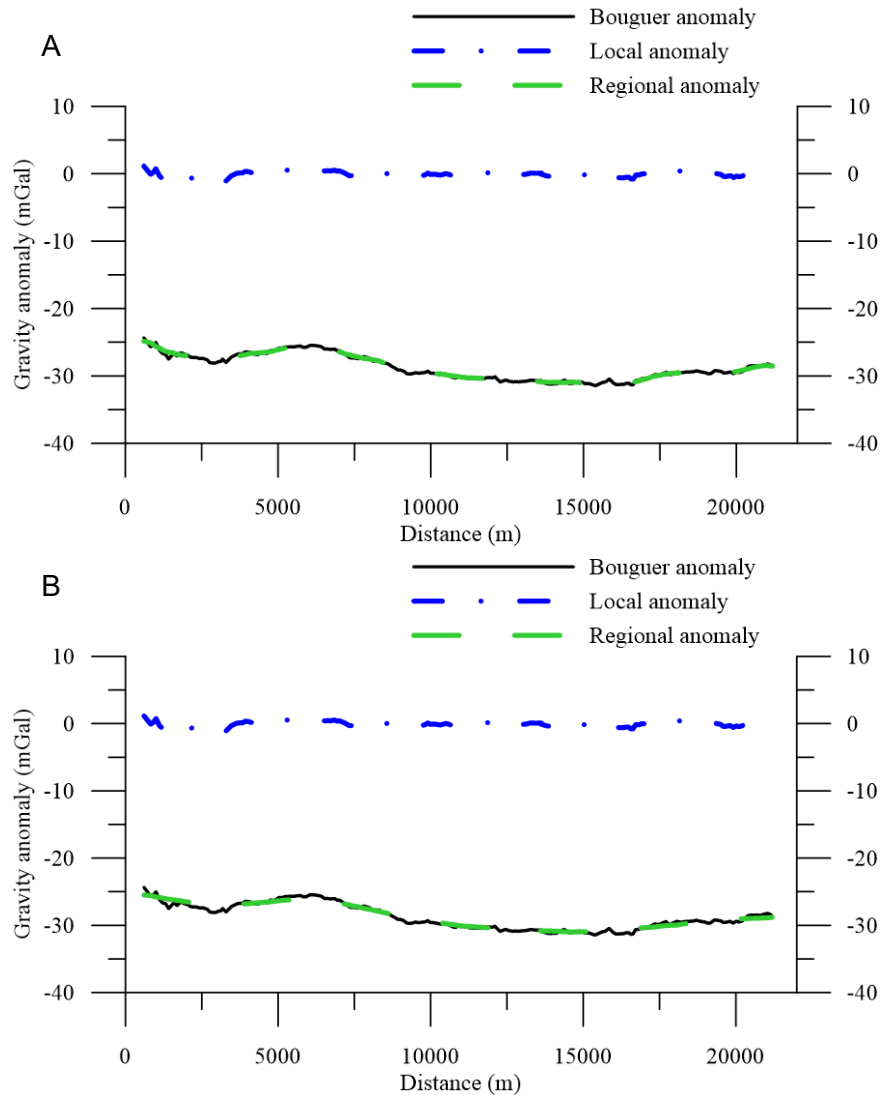
FIGURE 13: Separation of local and regional gravity anomalies:
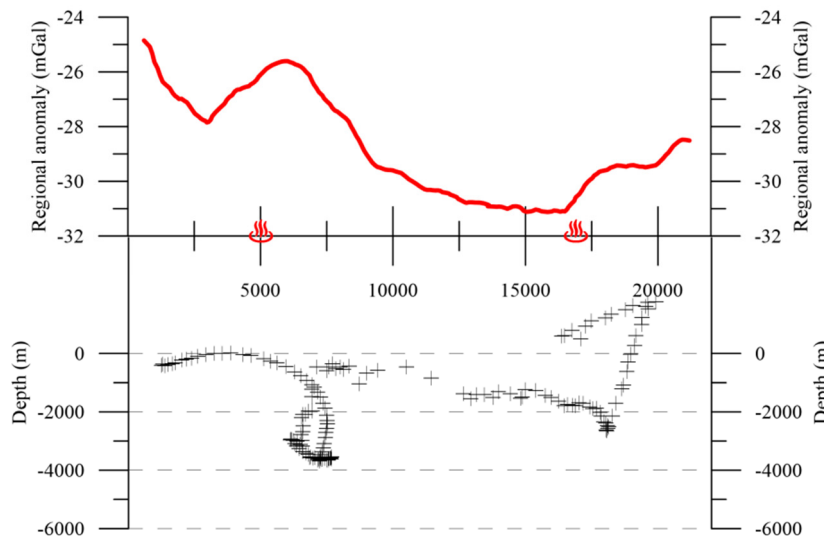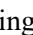A) window size of 10 points; B) window size of 40 points

FIGURE 14: Euler deconvolution results for the regional Bouguer anomaly;
black plusses show the position of the density anomaly; ♨ is a natural thermal spring

5.4 Inversion

5.4.1 Half-amplitude estimation

The half-amplitude formula is an easy way for maximum depth estimation in gravity (Liu, 2009). For a vertical cylinder the half-amplitude formula estimates the depth to the centre of a cylinder equal to the width of the anomaly at half amplitude. The width of the main anomaly between 2.5 and 10 km at half amplitude is 3.1 km, which is the depth down to the centre of the anomalous body according to this method.

5.4.2 Density tomography

The density imaging method is similar to seismic tomography and resistivity imaging methods. Underground strata are divided into a large number of rectangular cells with constant densities, and the final density distribution is obtained by minimizing a model objective function subject fitting to the observed data (Li and Oldenburg, 1998). The objective function is established in the spatial domain and solved by an optimal inversion method. By this, a 2D distribution of density of the underground medium is obtained. Density imaging can invert for density bodies in complex geological conditions, and the inversion process is automatic, which avoids the subjectivity of the inversion personnel.

The Bouguer anomaly is negative in the study area because the profile is on a thick continental crust. Because it is parallel with the major tectonic direction, the Moho variation along the profile should not be very significant. In order to remove the negative anomaly and make sure the residual density is positive, 37 mGal are added to the Bouguer anomaly after testing. The inverted depth is set as 7 km. Density variation is set as 0-0.4 g/cm^3 above the host rock density. After 23 iterations, the difference between the observed data and forwarded data was calculated to be 2.96%.

The density shown in Figure 15 is the residual density, meaning the density difference from the normal strata of the study area. An obvious high density (about 0.4 g/cm^3) is seen at the beginning of the profile, responsible for the high Bouguer anomaly there. A high-density anomaly of about 0.25 g/cm^3 is seen at
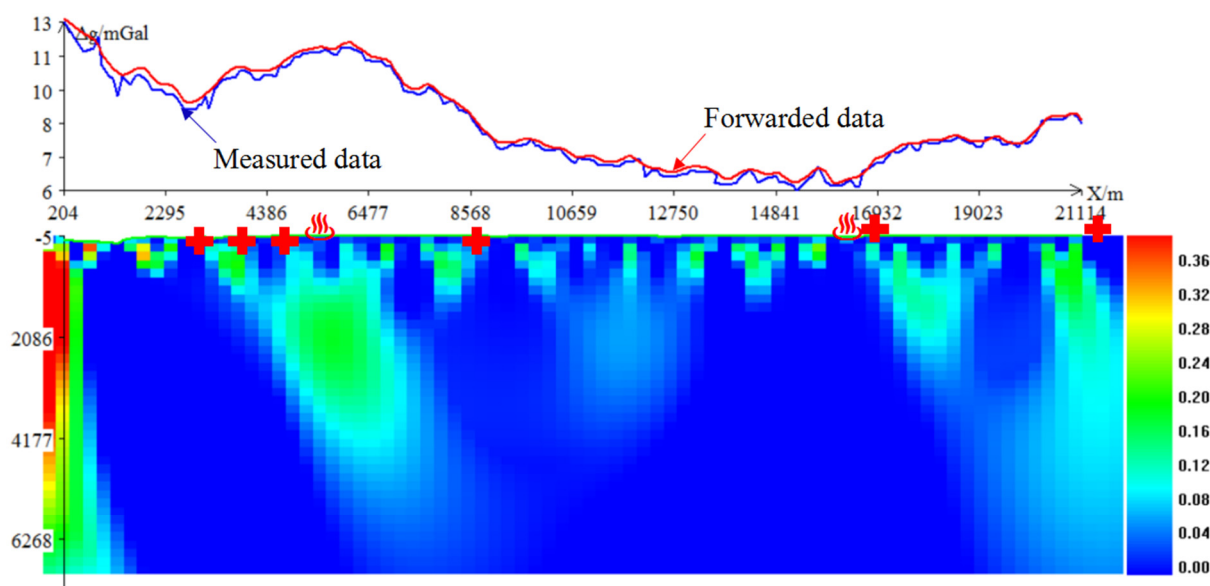

FIGURE 15: Density tomography of the gravity profile; the blue line is the observed Bouguer anomaly and the red line is the forward calculated data from the model below; the vertical scale of the model is in m below sea level, the unit of colour bar is residual density in g/cm^3;

♨ : Natural thermal spring; ✚ : Outcrops of intrusive rocks

4-6.5 km along the profile. It extends down to about 4 km depth. Here, outcrops of Cretaceous intrusive rocks are found and springs at the surface. This density anomaly is dipping to northeast. The range of the density anomaly under the Jurassic intrusive rocks at 8.5 km is small and mainly close to the surface. There are some small density anomalies near the surface between 9 and 15 km along the profile. And there is a density anomaly at 16 km where a Cretaceous intrusion and natural springs are located, tipping to the northeast beneath the surface.

6. BOREHOLE LOGS

The fault with northeasterly direction (F1), and the one with northwesterly direction (F3) meet in the region, forming the basic structural pattern as well as controlling the of distribution of hot springs in the area (Figure 2). A decision was made to drill a borehole in the area, with the purpose to study subsurface temperatures for geothermal exploration. The selected drill site is located at the north-eastern end of the ≥ 70°C hot spring area in the Zhangzhou-Xiamen geothermal field, surrounded by hot springs and near the intersection of the F1 and F3 faults (Figure 2). The terrain is relatively low, and the basement rock is intrusive granite of Mesozoic age. This area belongs to the uplifting part of the Moho surface in SE-China.

The 2009 m deep borehole was finished in 2017 with logging carried out after its completion. The main lithology of the borehole shows granite below 200 m with a small number of fracture intervals. The resistivity log shows general increases in resistivity with depth. Resistivity is around 400 Ωm at a depth of 400 m, and increases to about 1600 Ωm at a depth of 1600 m (Figure 16). There are little variations in the acoustic wave velocity. The natural self-potential has no obvious anomaly, and the natural gamma value is overall stable.

In order to get reliable information about thermal conditions, three temperature logs were carried out in the borehole. The first temperature log was run on July 3rd, 2017, with the highest measured temperature being 69.73°C at 2006 m. The second temperature logging was carried out on July 4th, 2017, with the highest measured temperature 70.15°C at 2002 m. Finally, the third log on July 5, 2017, showed the highest temperature of 70.4°C at 2005 m (Figure 17). Below 200 m depth, the temperature increases linearly with depth showing that the heat flow is controlled by conduction and no signs are seen of convection heat transfer.

FIGURE 16: Resistivity log of the borehole in Xinglin Bay geothermal field

The temperature log of the 3rd run can be used to calculate the thermal gradient. The temperature is 33°C at 255 m depth, and 70°C at 2000 m depth. The temperature gradient is $\Delta T/\Delta Z = (70-33)°C / (2000-255)m = 21.2°C/km$. This can be compared to the global mean temperature gradient 25-30°C/km according to Fridleifsson et al. (2008). The temperature gradient in the borehole is therefore in the range of the global average and much lower than the previously published temperature gradient in Zhangzhou Basin of 85-162.15°C/km (Yuan et al., 2006). Typical thermal conductivity of local rocks is between 2.93~3.35 W/m·K, and conductivity of granite in southeast China is 3.15±0.32 W/m·K (Xiong et al.,
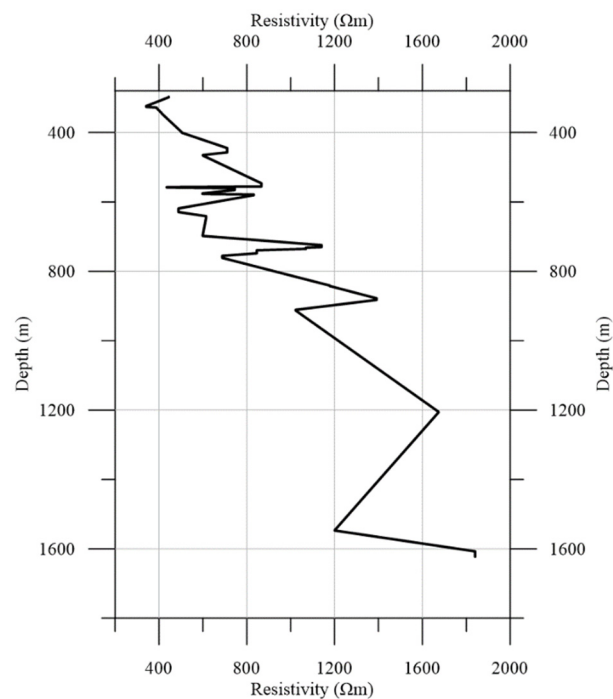
FIGURE 17: Temperature log of the borehole
in Xinglin Bay geothermal field

1994). The average conductivity of granite is used for heat flow calculation, because the major lithology in the borehole is granite. Surface heat flow from the borehole is 21.2 K/km×3.15 W/m·K = 66.78 mW/m². The global mean continental heat flow is 64.7 mW/m² (Davis, 2013) which is close to the heat flow around the borehole.

There are several heat flow measurements in the area. The highest published heat flow in Zhangzhou Basin is 209 mW/m² (Wang and Huang, 1990; Yuan et al., 2006), while the temperature gradient was reported as 85±26°C/km and thermal conductivity is 2.46±0.23 W/m·K. Other high heat flow measurements in Zhangzhou Basin were also checked. It is clear that the main reason for the previously published high heat flow relates to the high temperature gradient. One possible reason for the high temperature gradient is that the site of drilling was chosen near geothermal anomalies, driven by the possibility of geothermal utilization (Davies, 2013). The thermal springs in the Zhangzhou Basin are probably due to deep circulation of meteoric water in fractures in the basement rocks causing local high-temperature gradient anomalies. The abundance of hot springs and reported high temperature gradients is deep tectonic activity, which is abnormally high in the area. The heat flow values are not corrected for fluid advection, so they reflect local heat flow. The previously measured heat flow is possibly biased to higher values. The heat flow estimated from the borehole in this study probably reflects the regional geothermal background, and shows that it is not as high as previously considered. It is therefore concluded that the temperature gradients are variable and reflect local condition. The gradient is high close to the hot springs and fractures conveying geothermal water. Hence, shallow temperature gradient surveys could be very useful for geothermal exploration.

7. INTERPRETATION AND DISCUSSION

The geological structure of the Xinglin geothermal field was studied with MT and gravity measurements. Geothermal interpretation of the geophysical data is shown in Figures 18-20. The intrusive rocks are seen as high-resistivity and high-density features, and the results of the two methods agree in general. The intrusive rocks are exposed on the surface because of the complex geological movements in the study area. This is confirmed by surface outcrops of intrusive rocks and geothermal manifestations.

Hydrothermal studies were mainly focused on central part of the Zhangzhou Basin. Analysis of hot water shows high salinity and high Cl content, mainly due to the mixing of fresh water and sea water. The steam composition of the hot water is meteoric. The study of isotopes shows that the hot water originates from atmospheric precipitation, but it is affected by seawater mixing that results in isotope composition change (Xiong et al., 1990b). The recharge area estimated from the isotope elevation effect is the mountainous area around the basin, mainly in the northwest part, with an elevation of 800-1000 m. The hot water contains the radioactive isotope ^3H showing that it was replenished 30 years ago. The
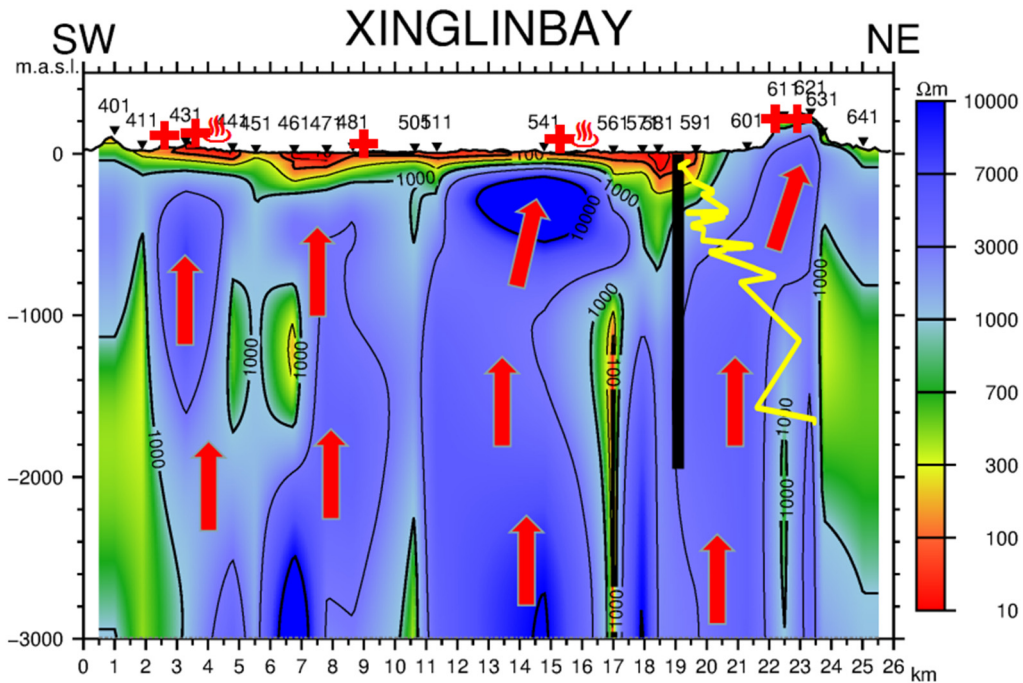
FIGURE 18: Interpretation of the resistivity cross-section; red arrows show the intrusion paths;
the black line shows the location of the borehole and the yellow line shows the resistivity log;
♨ : Natural thermal spring ✚ : Outcrop of intrusive rocks

reservoir temperature calculated by the hybrid SiO_2 thermometer is 140°C, the circulation depth is about 3.5-4 km deep. The temperature gradient is 30-35°C/km from the reservoir temperature and circulation depth (Xiong et al., 1990b).

A previous local study attributed the heat source of natural springs in Zhangzhou Basin to two major components: the heat generated by high radioactive granite in the upper crust and the deep heat from mantle (Wu et al., 2018). The presence of anomalous low-resistivity zones from the MT work is
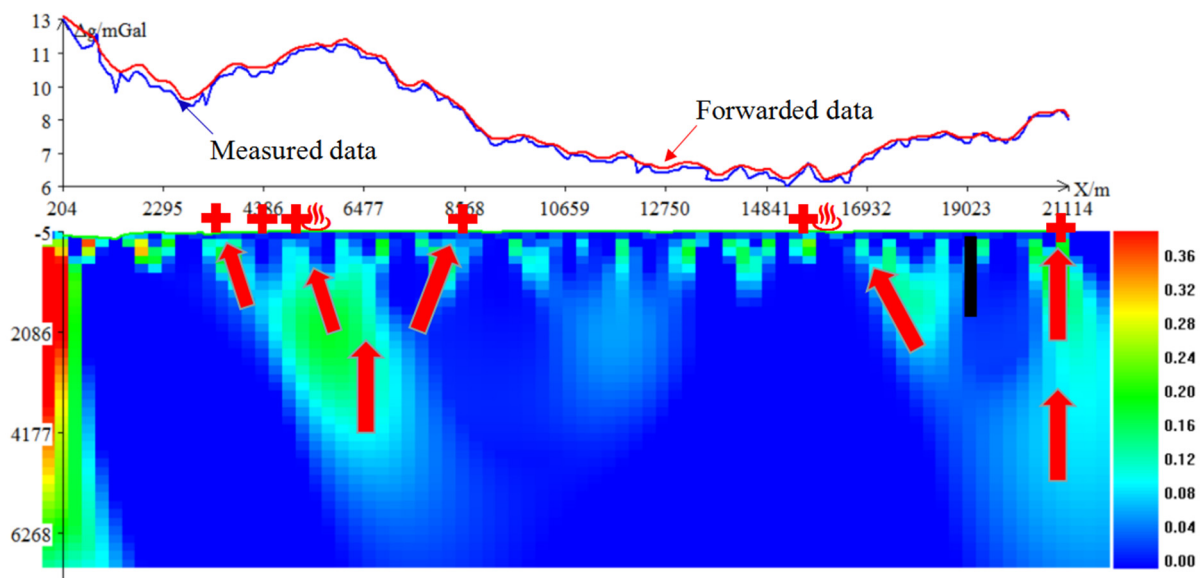

FIGURE 19: Interpretation of the gravity profile; red arrows show the intrusion paths;
the black line shows location of the borehole;
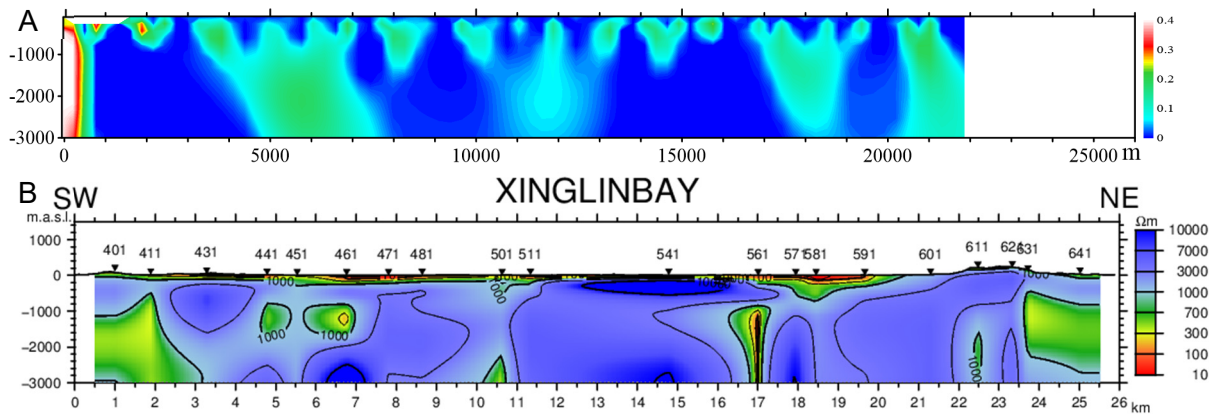♨ : Natural thermal spring; ✚ : Outcrop of intrusive rocks

FIGURE 20: Joint interpretation of a) Density; and b) Resistivity

considered to be due to molten materials formed in the Cenozoic times (Wu et al., 2018) in the volcanic belt along the southeast coastline, a part of the Pacific tectonic-magmatic belt. Cenozoic volcanic rocks are widely distributed in this region. In our study, the previously reported high heat flow may reflect local anomalies. The background heat flow is close to the global average value, not as high as previously considered. The strata have low permeability in general, but have fractures from intrusions and tectonic movements. The geothermal activity is mainly due to deep circulation of atmospheric precipitation in the deep granodiorite body with fracture permeability.

Resistivity surveying is generally considered a direct method for geothermal exploration. This method is more suitable for geothermal anomalies of high-temperature geothermal systems. The resistivity structure in mid to low-temperature geothermal systems is different from high-temperature geothermal systems because the temperature and permeability in the near-surface is not high enough to form substantial alteration. The most direct way for geothermal exploration in mid to low-temperature geothermal fields should be through temperature gradient surveying in shallow boreholes. Recommended locations of temperature gradient wells are shown in Figure 21. In our study area, natural springs are located in sediments near contact zones between intrusive rocks and the surrounding strata. The natural springs are exposed along fault F1, which is also parallel with the major tectonic direction. We suggest to investigate the temperature gradient along the line of natural springs and perpendicular to the F1 fault, then make the position of highest gradient as a deep borehole target.

8. CONCLUSION AND RECOMMENDATIONS

Geophysical work including MT, gravity and borehole logging was carried out in the Xinglin Bay geothermal field. MT and gravity data were processed and inverted. Joint interpretation of MT and gravity data was carried out and borehole logging carried out. The subsurface intrusions show up as high-resistivity and high-density anomalies. Surface heat flow in the study area, based on the temperature gradient measured in an exploration well is about 66.78 mW/m^2, which is not as high as previous estimates. The previously published high heat flow is probably biased towards higher values because the temperature gradient is affected by local fluid circulation.

The study area hosts fracture controlled low-temperature convection geothermal systems. The results of this geophysical work show that identification of geothermal systems in similar geological settings should mainly rely on methods which focus on fractures and intrusions, looking for convection of hot water through deep fractures.

Geophysical studies play an essential role in geothermal exploration, but has its limitations. Data quality is essential. For example, the success of MT measurements is strongly affected by data quality. In this
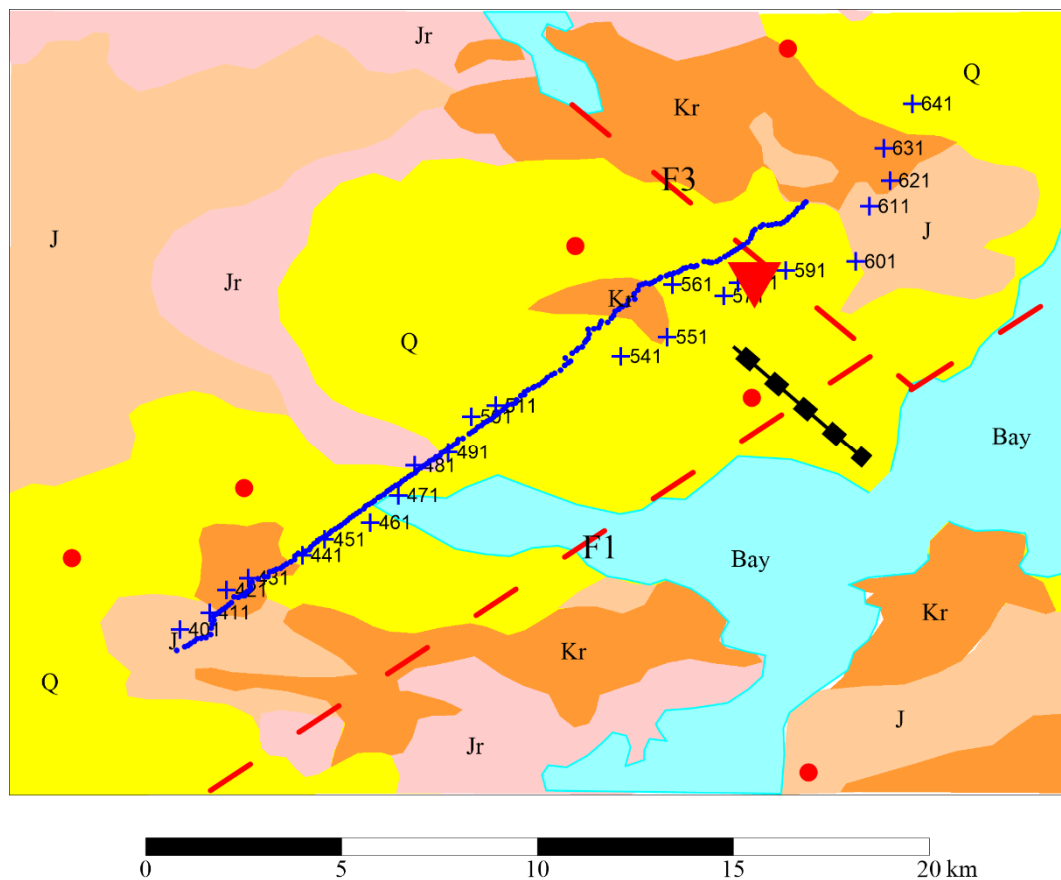
FIGURE 21: Recommended profile for temperature gradient survey,
suggested well sites shown as black rectangles

study the results are severely affected by static shift. Positions of MT stations should be chosen carefully in future work, and co-located TEM soundings should be done to correct the static shift and improve the MT data.

Resistivity surveying, which is normally considered a direct method in geothermal exploration, works better in high-temperature geothermal exploration where geothermal alteration forms a distinctive resistivity structure, associated with the geothermal activity.

In the case of the present study of deep circulation geothermal resources, the resistivity survey carried out does not give a clear picture of the geothermal activity. A more direct and appropriate approach would be to use shallow temperature gradient boreholes.

The geophysical survey discussed here is not conclusive for the geothermal exploration. Drilling of temperature gradient wells is recommended and sites suggested to be drilled before additional future deep drilling.

ACKNOWLEGEMENTS

help both in work and life in Iceland. They made my life much easier in the past months. I wish to give my thanks to all the lecturers during this training programme for the comprehensive presentations and willingness to share their knowledge and experience.

I would like to thank Mr. Knútur Árnason (ÍSOR, Iceland GeoSurvey) as my main supervisor, for his guidance. Also I have to thank Mr. Gylfi Páll Hersir (ÍSOR), who was in charge of the geophysical group during the whole course and gave precious advice to this study, as well as Ms. Ásdís Benediktsdóttir (ÍSOR) who was very patient with us. I also would like to thank Wu Chaofeng and Zhao Yabo, who are my Chinese colleagues and have been helping me with data processing and sharing important information with me.

I would like to thank my co-geophysical fellows this year. They are Makoye Mabula Didas, Jeffrey Gusman Sayco and Tsegaye Wondifra Tadesse. We had a lot of useful group discussions and they took very good care of me, especially in the field trip. I enjoyed working closely with them for three months.

Finally, I would like to thank all the UNU-GTP 2018 Fellows for the companionship. They highlighted my life in Iceland. It's been an amazing time for me and will be my best memory for my future life.

REFERENCES

Ai, Y., Chen, Q., Zeng, F., Hong, X., and Ye, W., 2007: The crust and upper mantle structure beneath southeastern China. earth *and Planetary Science Letters*, *260-3/4*, 549-563.

AQICN, 2018: *Air pollution in world: real-time air quality index visual map*. AQICN, website: *aqicn.org/map/china/#@g/31.1821/107.2705/4z*.

Árnason, K., 1989: *Central loop transient electromagnetic soundings over a horizontally layered earth*. Orkustofnun, Reykjavik, report OS-89032/JHD-06, 129 pp.

Árnason, K., 2006: *TEMTD. A program for 1D inversion of central-loop TEM and MT data. Short manual*. ÍSOR – Iceland GeoSurvey, Reykjavík, internal report, 17 pp.

Árnason, K., 2015: The static shift problem in MT soundings. *Proceedings of the World Geothermal Congress 2015 Melbourne, Australia,* 12 pp.

Blakely, R.J., 1995: *Potential theory in gravity and magnetic applications*. Cambridge University Press, 441 pp.

Chave, A.D., and Jones, A.G., 2012: *The magnetotelluric method: Theory and practice*. Cambridge University Press, 552 pp.

Constable, S.C., Parker, R.L., and Constable, C.G., 1987: Occam's inversion: A practical algorithm for generating smooth models from electromagnetic sounding data. *Geophysics*, *52-3*, 289-300.

Davies, J.H., 2013: Global map of solid earth surface heat flow. *Geochemistry, Geophysics, Geosystems*, *14-10*, 4608-4622.

Flóvenz, Ó., Hersir, G., Saemundsson, K., Ármannsson, H., and Fridriksson, T., 2012: Geothermal energy exploration techniques. In: Sayigh, A, (ed.): *Comprehensive renewable energy*, *7*. Elsevier, Oxford, 51-95.

Fridleifsson, I.B., Bertani, R., Huenges, E., Lund, J.W., Ragnarsson, A., and Rybach, L., 2008: The possible role and contribution of geothermal energy to the mitigation of climate change. *Proceedings of the IPCC scoping meeting on renewable energy sources, Luebeck, Germany*, Citeseer, 59-80.

Gamble, T.D., Goubau, W.M., and Clarke, J., 1979: Magnetotellurics with a remote magnetic reference. *Geophysics*, *44-1*, 53-68.

Geralda, D., Reid, A., and McInerney, P., 2004: New discrimination techniques for Euler deconvolution. *Computers & Geosciences*, *30-2*, 461-469.

Hersir, G.P., and Björnsson, A., 1991: *Geophysical exploration for geothermal resources, principles and applications.* UNU-GTP, Iceland, report 15, 94 pp.

Hirt, C., Claessens, S., Fecher, T., Kuhn, M., Pail, R., and Rexer, M., 2013: New ultrahigh-resolution picture of earth's gravity field. *Geophysical Research Letters*, *40-16*, 4279-4283.

Hu, X., Liu, S., Wu, C., and Yang, B., 2017: *Report on geophysical exploration of Xiamen Bay-Zhangzhou Basin on the west coast of the Straits*. China University of Geosciences, unpubl. report, 175 pp.

Lee, T.J., Song, Y., and Uchida, T., 2007: Three-dimensional magnetotelluric surveys for geothermal development in Pohang, Korea. *Exploration Geophysics*, *38-1*, 89-97.

Li, Y., and Oldenburg, D.W., 1998: 3-D inversion of gravity data. *Geophysics*, *63-1*, 109-119.

Liao, Q., Wang, Z., Wang, P., Yu, Z., Wu, N., and Liu, B., 1988: Explosion seismic study of the crustal structure in Fuzhou-Quanzhou-Shantou region. *Chinese J. Geophysics, 31-3 (in Chinese with English abstract)*, 270-280.

Liu, G., Han, K., and Han, J., 2012: Lithosphere electrical structure in southeast coastal region, South China. *J. Jilin University (earth Science Edition), 42-2* (in Chinese), 536-544.

Liu, T., 2009: *Instruction of GMS 3.0, a software for gravity and magnetic exploration* (in Chinese). China University of Geosciences, Wuhan, 177 pp.

Pavlis, N.K., Holmes, S.A., Kenyon, S.C., and Factor, J.K., 2012: The development and evaluation of the earth gravitational model 2008 (EGM2008). *J. Geophysical Research: Solid Earth*, *117-B4*.

Phoenix Geophysics, 2005*: V5 system 2000 MTU/MTU-A data processing – A user guide*. Phoenix Geophysics, Ltd., Toronto. Press Ltd., Oxford, 527 pp.

Reid, A.B., Allsop, J., Granser, H., Millett, A.t., and Somerton, I., 1990: Magnetic interpretation in three dimensions using Euler deconvolution. *Geophysics*, *55*, *1*, 80-91.

Stavrev, P.Y., 1997: Euler deconvolution using differential similarity transformations of gravity or magnetic anomalies. *Geophysical Prospecting*, *45-2*, 207-246.

Thompson, D., 1982: EULDPH: A new technique for making computer-assisted depth estimates from magnetic data. *Geophysics*, *47-1*, 31-37.

Unsworth, M., Soyer, W., Tuncer, V., Wagner, A., and Barnes, D., 2007: Hydrogeologic assessment of the Amchitka Island nuclear test site (Alaska) with magnetotellurics. *Geophysics*, *72-3,* B47-B57.

Vozoff, K. 1991: The magnetotelluric method. *Society of Exploration Geophysicists, Electromagnetic Methods in Applied Geophysics, 2, Application, Parts A and B*, 641-712.

Wan, T., 2012: *The tectonics of China: data, maps and evolution.* Springer Science & Higher Education Press, Beijing, 493 pp.

Wang, J., and Huang, S., 1990: Compilation of heat flow data in the China continental area (2nd ed.). *Seismology and Geology, 12-4* (in Chinese with English Abstract), 351-366.

Worzel, J.L., and Shurbet, G.L., 1955: Gravity interpretations from standard oceanic and continental crustal sections. *Crust of the earth: Geol Soc America, Special Paper*, *62*, *762*, 87-100.

Wu, C., Hu, X., Wang, G., Xi, Y., Lin, W., Liu, S., Yang, B., and Cai, J., 2018: Magnetotelluric imaging of the Zhangzhou Basin geothermal zone, Southeastern China. *Energies*, *11-8*, 2170, 1-15.

Xi Yufei, 2018: *Appendices to the report: Geophysical exploration in the Xinglin Bay geothermal field, SE-China.* UNU-GTP, Iceland, report 30 Appendices, 35 pp.

Xiong, L., Hu, S., and Wang, J., 1994: Analysis on the thermal conductivity of rocks from SE China. *Acta Petrologica Sinica, 10-3* (in Chinese with English abstract), 323-329.

Xiong, L., Wang, J., and Pang, Z., 1990a: Convective and conductive heat flows in Zhangzhou geothermal field, Fujian province, China. *Chinese J. Geophysics, 6* (in Chinese with English abstract), 703-711.

Xiong, L., Wang, J., and Pang, Z., 1990b: Circulation depth of the thermal water in Zhangzhou geothermal field. *Scientia Geologica Sinca, 4* (in Chinese with English abstract), 377-383.

Yang, J., Min, D.-J., and Yoo, H.-S., 2010: Sea effect correction in magnetotelluric (MT) data and its application to MT soundings carried out in Jeju Island, Korea. *Geophys. J. Internat., 182-2*, 727-740.

Yuan, X., Zuo, Y., Cai, X., and Zhu, J., 1989: The structure of the lithosphere and the geophysics in the South China Plate. *Progress on Geophysics in China in the 1980s, Editorial board of Bulletin of Geophysics* (in Chinese with English abstract), 243-249.

Yuan, Y., Ma, Y., Hu, S., Guo, T., and Fu, X., 2006: Present-day geothermal characteristics in South China. *Chinese Journal of Geophysics, 49-4*, (in Chinese with English abstract), 1005-1014.

Zhang, Z., and Wang, Y., 2007: Crustal structure and contact relationship revealed from deep seismic sounding data in South China. *Physics of the earth and Planetary Interiors*, *165- 1/2*, 114-126.

Zhou, L., Xie, J., Shen, W., Zheng, Y., Yang, Y., Shi, H., and Ritzwoller, M.H., 2012: The structure of the crust and uppermost mantle beneath South China from ambient noise and earthquake tomography. *Geophysical J. International*, *189-3*, 1565-1583.

Zhou, X., Sun, T., Shen, W., Shu, L., and Niu, Y., 2006: Petrogenesis of Mesozoic granitoids and volcanic rocks in South China: a response to tectonic evolution. *Episodes*, *29-1*, 26.